

# Ion-to-Neutral Ratios and Thermal Proton Transfer in Matrix-Assisted Laser Desorption/Ionization

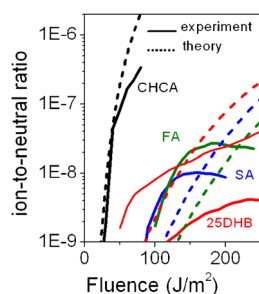
I-Chung Lu,<sup>1</sup> Kuan Yu Chu,<sup>1,2</sup> Chih-Yuan Lin,<sup>1</sup> Shang-Yun Wu,<sup>1</sup> Yuri A. Dyakov,<sup>1</sup> Jien-Lian Chen,<sup>1</sup> Angus Gray-Weale,<sup>3</sup> Yuan-Tseh Lee,<sup>1,2</sup> Chi-Kung Ni<sup>1,4</sup>

<sup>1</sup>Institute of Atomic and Molecular Sciences, Academia Sinica, Taipei, 10617, Taiwan

<sup>2</sup>Department of Chemistry, National Taiwan University, Taipei, 10617, Taiwan

<sup>3</sup>School of Chemistry, University of Melbourne, Melbourne, VIC 3010, Australia

<sup>4</sup>Department of Chemistry, National Tsing Hua University, Hsinchu, 30013, Taiwan



**Abstract.** The ion-to-neutral ratios of four commonly used solid matrices,  $\alpha$ -cyano-4-hydroxycinnamic acid (CHCA), 2,5-dihydroxybenzoic acid (2,5-DHB), sinapinic acid (SA), and ferulic acid (FA) in matrix-assisted laser desorption/ionization (MALDI) at 355 nm are reported. Ions are measured using a time-of-flight mass spectrometer combined with a time-sliced ion imaging detector. Neutrals are measured using a rotatable quadrupole mass spectrometer. The ion-to-neutral ratios of CHCA are three orders of magnitude larger than those of the other matrices at the same laser fluence. The ion-to-neutral ratios predicted using the thermal proton transfer model are similar to the experimental measurements, indicating that thermal proton transfer reactions play a major role in generating ions in ultraviolet-MALDI.

**Keywords:** MALDI, Ionization mechanism, Thermal proton transfer, Ion-to-neutral ratio

Received: 25 August 2014/Revised: 15 February 2015/Accepted: 16 February 2015/Published Online: 8 April 2015

## Introduction

Although matrix-assisted laser desorption/ionization (MALDI) has been widely used in mass analysis [1, 2], choosing the appropriate matrix is crucial for successful MALDI mass analysis. The selection of a matrix remains a trial-and-error process because the ionization mechanism of MALDI remains unclear. The generation of the first ions remains the most controversial aspect of the ionization mechanism.

The ion-to-neutral ratio is a crucial parameter used to characterize the properties of MALDI, and has frequently been used to justify the theoretical models of solid state ultraviolet (UV)-MALDI. Several studies have used ion yield [3] or degree of ionization [4], which essentially represents the same properties as the ion-to-neutral ratio does [5]. Numerous studies have referenced five previous studies [6–10] for conducting ion-to-neutral measurements

in solid state UV-MALDI. However, one of these studies did not report an ion-to-neutral ratio [10]. In two of these five studies, the ion-to-neutral ratios were measured outside the typical MALDI conditions [6, 7]. The other two studies reported the ion-to-neutral ratio of the analyte to be  $2.5 \times 10^{-4}$  near the threshold, and  $10^{-7}$  ( $100 \text{ J/m}^2$ ) or  $5 \times 10^{-6}$  ( $400 \text{ J/m}^2$ ) for the ion-to-neutral ratio of the matrix [8, 9]. These two studies have revealed the difference between the ion-to-neutral ratio of the analyte and the ion-to-neutral ratio of the matrix.

Numerous studies have cited the values of the ion-to-neutral ratios reported in the four studies described above without specifying whether they were ion-to-neutral ratios of the analyte or ion-to-neutral ratios of the matrix [11–16]. In addition, the original ratios obtained in these four studies have ranged from  $2.5 \times 10^{-4}$  to  $10^{-7}$  (including the measurements taken outside typical MALDI conditions), but in numerous recently published articles [14–16], the values have changed to  $10^{-3}$ – $10^{-4}$  without being specified for the matrix or the analyte and without clear reasons for the change of values. In our previous report [17], we mentioned that using ion-to-neutral ratios without identifying whether they are for analytes or matrices may cause confusion. Consequently, possible errors may occur in the

**Electronic supplementary material** The online version of this article (doi:10.1007/s13361-015-1112-3) contains supplementary material, which is available to authorized users.

Correspondence to: Chi-Kung Ni; e-mail: cknii@po.iam.s.sinica.edu.tw

determination of the MALDI mechanism. For example, a thermal ionization of electronically excited matrix model [18] and an energy pooling model [3] predicted the ion-to-neutral ratio of the matrix to be  $10^{-3}$ – $10^{-4}$ . The ion-to-neutral ratios of the matrix predicted from these two models were approximately  $10^4$  times greater than those derived from numerous experimental measurements [4, 9, 17, 19]. The predicted values were only close to the ion-to-neutral ratios of the analyte for certain analytes but not the ion-to-neutral ratios of the matrix.

Recently, we reported the upper limit of ion-to-neutral ratios of the matrix for 2,5-DHB and ion-to-neutral ratios of the analyte for various analytes in 2,5-DHB at 355 nm [17]. The ion-to-neutral ratio of the matrix was approximately  $10^{-8}$  near the threshold and became  $3 \times 10^{-7}$  at increased laser fluences. The values of the ion-to-neutral ratios of the analyte for analytes with high proton affinity (bradykinin and tryptophan) were in the range of  $10^{-3}$ – $10^{-5}$ , and were less than  $10^{-8}$  for analytes with low proton affinity (glycine). The considerable difference between the ion-to-neutral ratios of the matrix and ion-to-neutral ratios of the analyte was clearly demonstrated in the study. We reported only the upper limit of the ratios because of two reasons. First, we did not know the absolute ion transmission efficiency of the quadrupole mass spectrometer in the desorbed neutral measurement. We set the mass resolution of the quadrupole mass spectrometer as low as possible to increase the transmission efficiency, and used the highest ion transmission efficiency (100%) in calculations, producing the lower limit of neutrals. Second, the desorbed neutrals generated from every laser shot were averaged. However, in the desorbed ion measurement, laser shots that did not produce any ions were excluded when the ion counts were averaged. This produced the upper limit of the ion counts.

In the present study, we calibrate the absolute transmission efficiency of the quadrupole mass spectrometer, consider every laser shot in calculating the average ion number, and improve the calculations of the dielectric constant in the thermal proton transfer model. We report the ion-to-neutral ratios of the matrix of four common solid state matrices,  $\alpha$ -cyano-4-hydroxycinnamic acid (CHCA), 2,5-dihydroxybenzoic acid (2,5-DHB), sinapinic acid (SA), and ferulic acid (FA) at 355 nm, and compared the results with the predicted values obtained using a thermal proton transfer model for solid state UV-MALDI [20, 21]. We chose these four common matrices because the absolute UV absorption coefficients of solid-state matrices at 355 nm, which is a crucial parameter in model calculations, are available [22].

## Experimental

The experimental methods for the detection of desorbed neutrals and ions were described in detail in a previous report [17]. Only a brief description is provided here. The calibrations of the absolute ion transmission efficiency of a quadrupole mass spectrometer are described in detail in this report.

### *Ion Detection*

The relative ion intensity of MALDI-grade and non-MALDI-grade materials is measured using a commercial time-of-flight mass spectrometer (Autoflex III; Bruker Daltonik GmbH, Bremen, Germany). The absolute numbers of ions generated through MALDI are detected using a home-made time-of-flight (TOF) mass spectrometer combined with an ion imaging system [17, 23, 24]. The number of ions are directly counted from the ion image or calculated from the image intensity detected using a photomultiplier tube (PMT). The experimental method was discussed in detail previously [17].

The 355-nm laser beam is provided by the third harmonic of a Q-switched Nd:YAG laser (Spectra Physics Lab 190, pulse duration approximately 7 ns). The energy of the laser beam is controlled by a 355-nm  $1/2\lambda$  wave plate and a polarizer. Energy is measured using a pyroelectric detector (Molelectron, J3-09). After entering the vacuum chamber, the laser beam is focused using a lens (fused silica,  $f=25$  cm). The spot size of the laser beam on the sample plate measured using the burn spot on the burn paper is 200  $\mu\text{m}$  in diameter.

### *Neutral Detection*

The desorbed neutral molecules are detected using a modified crossed molecular beam apparatus. Most of the details concerning the main chamber and detector chamber have been reported in previous studies [25, 26]. The details of the apparatus and the modifications made specifically for laser desorption studies have been described in previous reports [17, 27].

The desorbed neutral molecules are detected using a rotatable quadrupole mass spectrometer. The rotatable quadrupole mass spectrometer can detect neutral molecules desorbed from a surface in angles ranging from  $-15^\circ$  to  $90^\circ$  ( $0^\circ$  is defined as normal to the surface) with a resolution of  $1.5^\circ$ . The distance between the sample surface and the ionization region of the mass spectrometer is 35 cm. The velocity distribution of each desorbed neutral molecule is obtained from the arrival time of the ionized neutral at the detector of the mass spectrometer. The angular resolved distributions of the desorbed neutral products are obtained by rotating the mass spectrometer around the laser spot on the sample surface. The amount of neutral desorption is determined by integrating the angles, velocities, and masses.

Laser desorption not only changes the molecules from the condensed phase to the gas phase but occasionally also causes small pieces of the solid sample to eject from the sample surface. The kinetic energies of these small pieces are either not sufficiently large to fly into the detector within the observation time window or are too small, such that they fall to the bottom of the vacuum chamber before entering the ionization region. The advantage of this method is that these pieces of the solid sample can be distinguished from the gas-phase molecules. The gas-phase molecules, including monomers and small clusters, are detected; the small pieces of the solid sample are excluded.

Pulsed laser desorption is achieved using the third harmonic (355 nm) of an Nd:YAG laser (Minilite II; Continuum Inc., San

Jose, CA, USA; pulse duration approximately 7 ns). The laser light travels through a lens (fused silica,  $f=20$  cm) onto the sample surface with a  $45^\circ$  incident angle. The beam spot size is the same as the spot size used in ion detection.

When calibrating the absolute transmission efficiency of the quadrupole mass spectrometer, the sample holder is replaced by a tube (1 cm in diameter, 8 cm in length) containing Ar gas. One end of the tube is sealed by a thin stainless-steel (0.1-mm thick) with a hole that is 0.5 mm in diameter. The position of the hole is located at the same position as the laser spot on the MALDI solid sample surface. The other end of the tube is connected to a pressure meter, controller, and Ar gas cylinder. The pressure inside the tube is controlled using a pressure controller (type 250E-1-D; MKS Instrument Inc., Andover, MA, USA) and monitored using a Baratron capacitance manometer (type 722A 1 Torr, model no. 722A01TGA2FJ; MKS Instruments Inc.). Ar atoms diffuse from the hole at the bottom of the tube and enter the main chamber. A portion of the Ar atoms fly directly into the detection chamber and are detected by the rotatable quadrupole mass spectrometer. Ar atoms that do not fly directly into the detection chamber are pumped out from the main chamber or differential pumped chamber.

### Sample Preparation

Both MALDI-grade and non-MALDI-grade materials are investigated in this study. The MALDI-grade materials are purchased from Sigma Aldrich; for the non-MALDI-grade materials, 2,5DHB and SA are purchased from Acros Organics, Geel, Belgium and CHCA and FA are purchased from Sigma Aldrich. Details of the chemicals are described in the [Supplementary Material](#). All the chemicals are used without further purification. Matrix stock solutions are prepared by dissolving the corresponding compounds separately in a 50% acetonitrile aqueous solution. The solution is vacuum-dried evenly on the sample holder. The thickness of the sample after being vacuum-dried is approximately 300  $\mu\text{m}$ .

In both ion and neutral detection, the laser irradiation spot on the sample surface is located at the axis of the detection (TOF mass spectrometer or quadrupole mass spectrometer at  $0^\circ$ ). The rotation axis of the sample holder is offset by 4 mm from the axis of detection. This enables us to use a new sample surface for laser desorption by rotating the sample holder without breaking the vacuum.

## Results and Discussion

### Ions

*Comparison of MALDI-Grade and Non-MALDI-Grade Materials* Table 1 shows the relative ion intensities for MALDI-grade (>99%) and non-MALDI-grade (> 98%) materials. The uncertainty represents the fluctuation of ion intensity. The uncertainty is partially caused by the inhomogeneous sample surface and the fluctuation of the MALDI signal. The results show that the ion intensities of the MALDI-grade and

**Table 1.** The Relative Ion Intensities for MALDI-Grade (>99%) and Non-MALDI-Grade (>98%) Materials

Sample	1	2	3	4	5	6	7	8	9	10
Material	MALDI	non- MALDI	MALDI	non- MALDI	MALDI	non- MALDI	MALDI	non- MALDI	MALDI	non- MALDI
SA	202±38	179±46	168±31	122±14	299±37	147±33	251±42	99±17	226±31	216±46
FA	41±2	54±9	65±12	49±11	68±13	67±20	91±21	41±2	68±18	72±16
CHCA	179±12	130±11	171±15	137±12	151±12	197±29	162±19	111±8	190±15	169±18
25DHB	126±23	138±27	490±156	142±16	257±44	163±29	409±178	223±87	336±145	270±100

For each matrix, the experiments were repeated five times (five samples). We randomly chose 20 positions on each sample, and mass spectrum was accumulated for the first 10 laser shots for each position. Each datum represents the accumulation from 200 laser shots. The uncertainty represents the fluctuation of ion intensity.

non-MALDI-grade materials used in this study have similar orders of magnitude, and that most of the differences in ion intensity are caused by experimental uncertainty.

**Absolute Ion Number** We use CHCA as an example to demonstrate the data analysis. Figure 1 shows the ion images for  $m/z=172$   $[(\text{CHCA}-\text{H}_2\text{O})\text{H}^+]$  and  $190$   $[(\text{CHCA})\text{H}^+]$  and the TOF mass spectra obtained from pure solid CHCA samples. Each image is obtained using a single laser shot. No ions are distributed at the edge of the detector, indicating that all ions are collected by the ion optics and detected by the micro-channel-plate (MCP) detector. Two types of images are shown in Figure 1. Figure 1a shows the image of low ion counts. Each ion generates a bright spot on the image when it is detected by the ion imaging detector. The numbers of ions can be counted directly from the images. In addition, we measure the signal obtained from the fast-decay phosphor by using the PMT simultaneously. The signal from the PMT, representing the TOF mass spectra of the same laser shot, is shown in the right

column of Figure 1. The relationship between the ion counts from the image and the PMT output voltage is established from the average of many low ion count measurements.

As the number of ions increase, the images of the ions overlap. A typical image for a high number of ions from a single laser shot is shown in Figure 1b. The number of ions cannot be counted directly from this image. Consequently, the PMT output voltage from the same laser shot is used to calculate the number of ions according to the relationship between the ion count and PMT output voltage determined using low ion count measurements.

In calculating the total number of desorbed ions, the parameters used are the ion intensity ratio of detected ions ( $m/z=172$  and  $190$ ) to other ions, including  $m/z=164$   $[(\text{CHCA}-\text{CN})\text{H}^+]$ ,  $172$   $[(\text{CHCA}-\text{H}_2\text{O})\text{H}^+]$ ,  $190$   $[(\text{CHCA})\text{H}^+]$ , and  $379$   $[(\text{CHCA})_2\text{H}^+]$ , ion transmission efficiency of a fine metal mesh placed in front of the MCP (60%, BM-0400-01; Industrial Netting, USA, open area ratio of the MCP (63%), and the ion detection quantum efficiency of the MCP (60%–85% for the ion kinetic energy of 6.5 KeV used in this study [28]). The ion intensity ratio is fluence-

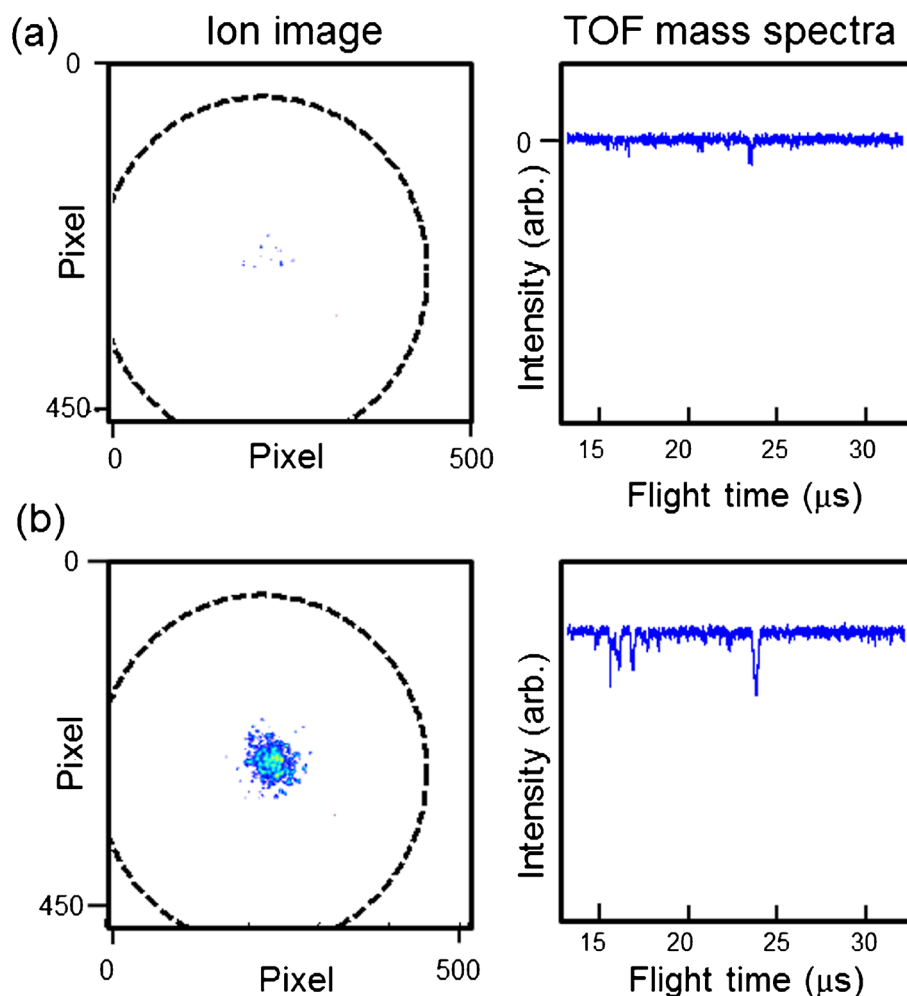


**Figure 1.** CHCA ion images and TOF mass spectra. Left column: ion image of  $m/z=172$  and  $190$  from a single laser shot. The large circle represents the detector size. Right column: signal from the PMT, representing the TOF mass spectra of the same laser shot. (a)  $30 \text{ J/m}^2$ , (b)  $40 \text{ J/m}^2$

dependent. The ion intensity of  $m/z=172$  and 190 is approximately 0.32 of the total ion intensity of the other ions, calculated using the TOF mass spectra at laser fluences of  $75 \text{ J/m}^2$ .

The number of ions, after being corrected using the parameters described previously, is plotted as a function of laser fluence. The result is shown in Figure 2. In this plot, only the related protonated matrix ions are considered. Ions unrelated to proton transfer, such as  $\text{Na}^+$ ,  $\text{K}^+$ , and sodiated matrix ions, are not included in Figure 2. Each data point in Figure 2 represents the averaged ion intensity derived from 100 laser shots. These 100 laser shots include 20 sample positions and five laser shots for each sample position.

Among these four matrices, the ion intensity of 2,5-DHB fluctuates significantly among the sample positions. Some positions generate numerous ions; some positions do not generate ions at all. The large fluctuation of ion intensity has been known for a long time, and it is related to the property of the “sweet spot.” In this study, we report the average desorbed ions of 2,5-DHB in two types. One type is that every laser shot is taken into average. The other type is that only the laser shots that generate ions are taken into average. The results of 2,5-DHB in both types are plotted in Figure 2. The difference between these two types is almost as large as two orders of magnitude at the laser fluence near the threshold, but it is reduced to less than one order of magnitude at high laser fluence.

## Neutrals

**Calibration of Detection Efficiency** When calibrating the detection efficiency of the quadrupole mass spectrometer, the MALDI sample holder is replaced by a stainless steel tube containing Ar. The acceptant angle of the ionizer in

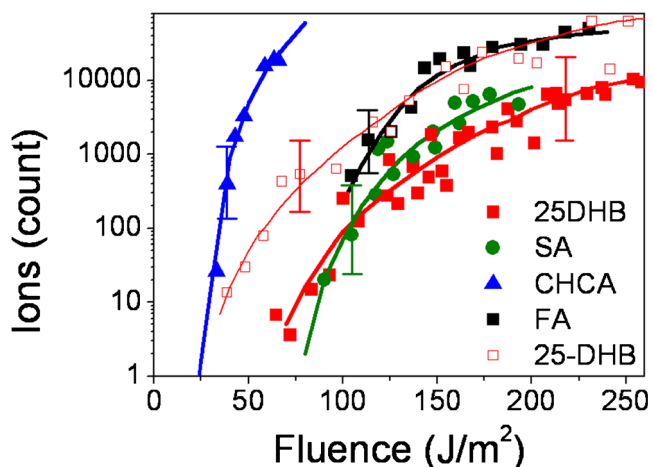


**Figure 2.** Desorbed ions as a function of laser fluence. Solid lines represent the fitting of the data to smooth curves. Solid squares represent every laser shot that is taken into average; open squares represent only the laser shots that generate ions taken into average

the quadrupole mass spectrometer is  $1.5^\circ$ . The Ar flux,  $[\text{Ar}]$ , from the hole of the tube to the ionizer within the time period  $\Delta t$  can be calculated using the theory of gas kinetics [29]:

$$[\text{Ar}] = \int_{v=0}^{v=\infty} \int_{\varphi=0}^{\varphi=180} \int_{\theta=0}^{\theta=0.75} n \times A \times v \times \Delta t \times \cos\theta \times \left(\frac{m}{2\pi kT}\right)^{3/2} \times \exp\left(-\frac{mv^2}{2kT}\right) \times v^2 \times \sin\theta \times dv d\varphi d\theta = n \times A \times \Delta t \times \langle v \rangle \times \left[\frac{\sin^2\theta}{2}\right]_0^{0.75}$$

The parameters  $n$ ,  $A$ ,  $v$ ,  $m$ ,  $k$ ,  $T$ , and  $\langle v \rangle$  represent the density of Ar inside the tube, area of the hole (0.5 mm in diameter), velocity and mass of the Ar atoms, Boltzmann constant, temperature (300 K), and average velocity of Ar atoms inside the tube (398 m/s), respectively.

The number of ions detected by the detector,  $[\text{Ar}^+]$ , depends on the flux of Ar,  $[\text{Ar}]$ ; the electron density in the ionization region,  $I_e$ ; the duration of the Ar atoms in the ionization region,  $\Delta t_i$ ; the Ar ionization cross-section,  $\sigma(\text{Ar})$ ; the ion transmission efficiencies of the ion optics and quadrupole mass filter,  $T_r$ ; and the quantum efficiency of the ion detector,  $Q$ :

$$[\text{Ar}^+] = I_e \times \Delta t_i \times \sigma(\text{Ar}) \times T_r \times Q \times [\text{Ar}] = c \times \Delta t_i \times \sigma(\text{Ar}) \times [\text{Ar}]$$

where  $c=I_e \times T_r \times Q$  represents the instrument characteristics. Comparing the Ar ions detected by the detector per second and the flux of Ar atoms derived from calculations enables the calculation of the entire ion detection efficiency. A total of  $1.3 \times 10^6$  Ar ions are detected within 1 s for 10 mTorr of Ar pressure inside the tube under the conditions of a given mass resolution and the given filament current of the ionizer (1 mA). The duration of the Ar atoms in the ionization region,  $\Delta t_i$ , is calculated using the length of the ionization region (3 cm) and the average velocity of the Ar atoms (398 m/s). Parameter  $c$  is determined to be  $5.7 \times 10^{13}$ , based on the Ar ionization cross-section  $\sigma=3 \times 10^{-16} \text{ cm}^2$  [30]. An additional correction factor of instrument characteristics is the mass-dependent transmission efficiency, which depends on the mass of fragments. Generally, the correction factor is approximately 1.5–1.9 for the matrices we studied [31].

**Desorbed Neutrals** We use CHCA as an example to demonstrate data analysis of the desorbed neutrals. The major ions of the mass spectra obtained using 70-eV electron ionization are  $m/z=189$ , 147, 117, 89, 39. A fragment ion intensity of  $m/z=89$  is approximately 3.2% of the total ion intensity at  $72\text{-J/m}^2$  laser fluence. The TOF spectra of desorbed neutral molecules measured from various angles are shown in Figure 3. They are obtained from ion  $m/z=89$  at laser fluences of 72 and  $136 \text{ J/m}^2$ . Intensities near  $0^\circ$  (normal to surface) are high. Generally,

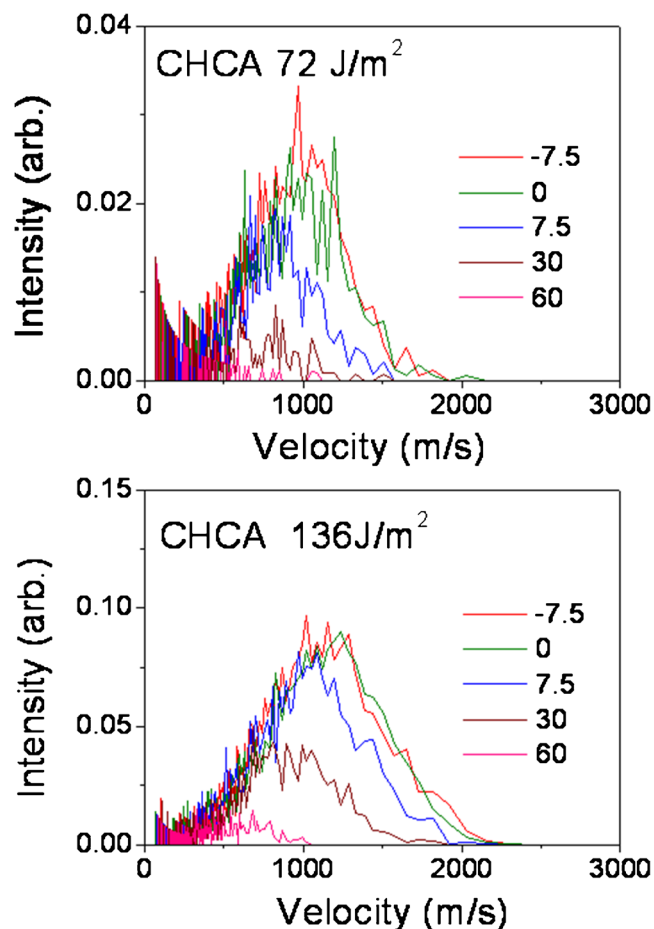


Figure 3. Velocity distributions of desorbed neutral species from the CHCA sample measured at different angles (in degrees). No signal is observed at angles more than 60°. When neutral CHCA molecules are ionized by 70-eV electrons, they crack into different ionic fragments. Only  $m/z=89$  is shown in this figure. The other ions exhibit a similar velocity and angular distributions

intensity and velocity increase as laser fluence increases, and the intensity decreases as the angle increases for a given laser fluence. Almost no signal is observed at more than 60°. The other ions exhibit a similar velocity and angular distributions.

The total amount of neutral desorption per laser shot is calculated using the following equation:

$$\begin{aligned}
 \text{Neutrals} = & \sum_{m/z} \int_{v=0}^{v=\infty} \int_{\varphi=0}^{\varphi=180} \int_{\theta=0}^{\theta=90} I_{m/z}(v, \theta, \varphi) \\
 & \times \frac{1}{c \times \Delta t_i \times \sigma(M)} \times \sin\theta \times v dv d\varphi d\theta
 \end{aligned}$$

where  $I_{m/z}$  is the ion counts at a given mass-to-charge ratio  $m/z$ , a given angle ( $\theta, \varphi$ ), and velocity  $v$ . In the experimental measurement of desorbed matrix neutrals, the mass

resolution and filament current are maintained at the same values as those used in the calibration of detection efficiency. The desorption laser beam and electron-impact ionization generate several fragments. The calculations include the summation of all possible fragments  $m/z$ . The duration of the neutrals in the ionization region,  $\Delta t_i$ , depends on the velocity of the neutrals. For simplicity, we use the average velocity derived from experimental measurements.

Ionization cross-sections of neutrals ionized by electron impact at 70 eV range from  $4 \times 10^{-17} \text{ cm}^2$  for small atoms such as He [32] to  $1.5 \times 10^{-15} \text{ cm}^2$  for large molecules such as benzene [33] or  $1.7 \times 10^{-15} \text{ cm}^2$  for hexan-3-one [34]. Ionization cross-sections can be estimated on the basis of the polarizability [34]. The estimated ionization cross-sections based on polarizability are  $3.4 \times 10^{-15} \text{ cm}^2$  (CHCA),  $2.2 \times 10^{-15} \text{ cm}^2$  (2,5-DHB),  $3.4 \times 10^{-15} \text{ cm}^2$  (FA), and  $3.8 \times 10^{-15} \text{ cm}^2$  (SA). These values are used in this study. The final results for the desorbed neutrals are illustrated in Figure 4.

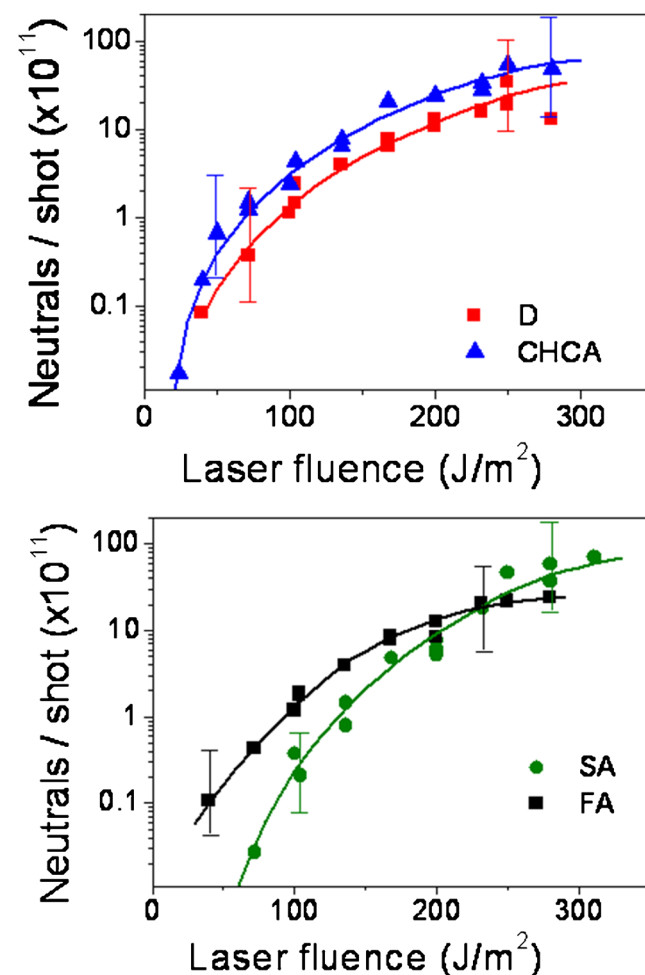


Figure 4. Desorbed neutrals (solid symbols) as a function of laser fluence. Solid lines represent the fitting of the data to smooth curves

### Ion-to-Neutral Ratios

The desorbed ions and neutrals described in previous sections are used to calculate ion-to-neutral ratios. Figure 5 shows the ion-to-neutral ratio as a function of laser fluence.

### Thermal Proton Transfer Model

The thermal proton transfer model was successfully used to describe the ion-to-neutral ratio of 2,5-DHB in our previous study [20, 21]. Knochenmuss criticized the thermal proton transfer model recently [35]. We demonstrate that Knochenmuss applied the calculations under inapplicable conditions and that we applied the calculations under a suitable condition [36]. These criticisms are discussed in a separate paper [36], and none of these criticisms are found to be valid in a MALDI process.

We apply this model to predict the ion-to-neutral ratios in this study. Details of the thermal proton transfer model and calculations were described in our previous report and [Supplementary Material](#). Only a brief description is provided here.

In the thermal proton transfer model, ions generated through MALDI are primarily produced by thermally induced proton transfer reactions at high temperatures. When the temperature increases and the solid sample turns into a liquid, proton transfer reactions reach equilibrium because of the low barrier height of the proton transfer reactions and high collision frequency between molecules in the liquid. In a pure matrix sample, the thermal proton transfer reaction can be represented by Reaction 1:

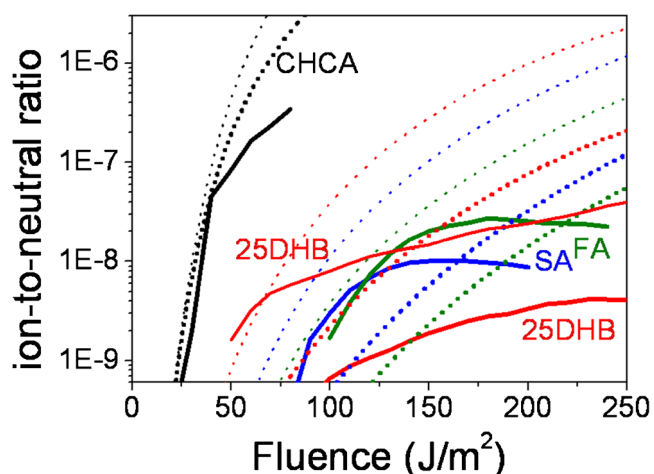
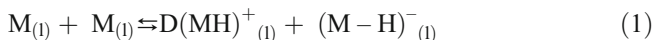
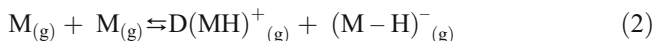


**Figure 5.** Ion-to-neutral ratios for four matrices (black: CHCA, red: 2,5-DHB, blue: SA, green: FA) as a function of laser fluence. Solid lines represent the experimental measurements; dotted lines represent the theoretical calculations from the thermal proton transfer model (see details below). Thick dotted line and thin dotted line represent the ion-to-neutral ratio when  $g=1$  and  $2$  are used in Equation 11, respectively

$M$ ,  $(MH)^+$  and  $(M-H)^-$  represent the matrix, protonated matrix, and deprotonated matrix, respectively. After desorption, the ion intensities of various species may change because of the reactions that occur in the gas plume.



However, ion generation caused by the proton transfer reaction (forward reaction in Reaction 2) and ion-ion recombination (backward reaction in Reaction 2) in the gas phase quickly stops occurring because of the rapid gas plume expansion in the vacuum. Numerical calculations indicate that the number of ions generated in the gas phase or the number of ions involved in recombination is extremely small, such that the ion-to-neutral ratio in the gas phase remains similar to the ratio in the liquid phase [20, 21].

The equilibrium constant  $K$  for Reaction 1 in the liquid phase can be written as follows:

$$K = \frac{[M-H]^- \times [M+H]^+}{M^2} = e^{-\frac{\Delta G_1}{RT}} \quad (3)$$

The Gibbs free energy for Reaction 1 is  $\Delta G_1$ . In accordance with the charge balance,  $[M-H]^- = [M+H]^+$ , the cation-to-neutral ratio or anion-to-neutral ratio can be derived from the square root of Equation 3:

$$\frac{\text{cation}}{\text{neutral}} = \frac{\text{anion}}{\text{neutral}} = \sqrt{K} = e^{-\frac{\Delta G_1}{2RT}} \quad (4)$$

Therefore, the cation-to-neutral ratio and anion-to-neutral ratio can be predicted if the Gibbs free energy and the temperature are known.

### Temperature

The temperature  $T$  in the irradiated volume prior to desorption can be described using the following heat equation:

$$F = \frac{\rho_0}{\alpha(1-\Phi)} \int_{T_0}^T c_p(T) dT + \Delta m(F) \times L \quad (5)$$

where  $\rho_0$ ,  $c_p$ ,  $\alpha$ ,  $\Phi$ ,  $T_0$ ,  $F$ ,  $\Delta m$ , and  $L$  denote the mass density before laser irradiation, specific heat capacity, absorption coefficient at 355 nm, fluorescence quantum yield of the solid matrix, initial temperature, laser fluence, desorbed molecules per unit area, and latent heat of fusion, respectively. The temperature-dependent heat capacity can be calculated on the basis of the molar heat capacity of the solid matrix by using a modified Einstein model and molecular vibrational frequencies from ab initio calculations. The details of the heat capacity calculations were described in a previous report [20, 21] and in the [Supplementary Material](#). The calculated heat capacity of SA and FA is slightly larger than that of CHCA, and 2,5-DHB exhibits the smallest heat capacity. This is because the number

of low vibrational frequency modes are in the order SA>FA>CHCA>2,5-DHB.

The mass density used in Equation 5 is measured using the volume change of the saturated matrix aqueous solution by adding a given weight (1.1–1.5 g) of the matrix powder into the solution. The fluorescence quantum yields of the solid matrix sample are measured using a commercial integrating sphere (Fluorescence Spectrometer, model: FLS 920; Edinburgh Photonics, Edinburgh Instruments Ltd., Livingston, UK) The absorption coefficients for solid matrices SA, FA, 2,5-DHB, and CHCA at 355 nm are  $1.25 \times 10^5 \text{ cm}^{-1}$ ,  $1.25 \times 10^5$ ,  $8.7 \times 10^4$ , and  $3.5 \times 10^5 \text{ cm}^{-1}$ , respectively [22]. The number of desorbed molecules per unit area is derived from the experimental measurements reported in this work. Typical latent heats of fusion for organic molecules exhibiting intermolecular hydrogen bonding are in the range of 10–30 kJ/mol [37]. The surface temperature  $T$ , calculated using Equation 5, is shown in Figure 6 and represents the maximal temperature before desorption occurs. The temperatures of these four matrices are ordered in the sequence  $T(\text{CHCA}) \gg T(\text{SA})=T(\text{FA}) > T(2,5\text{-DHB})$  because of the substantial difference in the absorption coefficients.

### Gibbs Free Energy

The Gibbs free energy for Reaction 1 in the liquid phase,  $\Delta G_1$ , can be derived using the Gibbs free energies of the following three reactions:

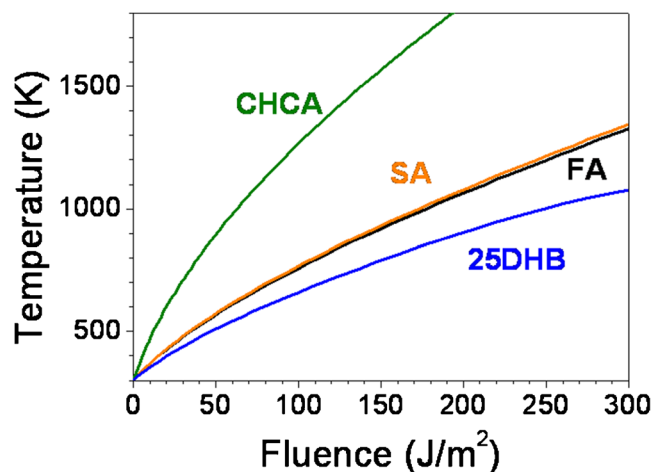
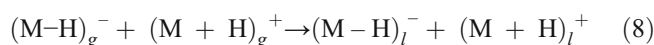
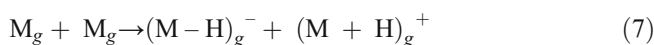


Figure 6. Calculated maximum surface temperature before desorption occurs

Subscripts  $g$  and  $l$  represent the gas and liquid phases, respectively. The Gibbs free energy relationship for these reactions is  $\Delta G_1 = \Delta G_6 + \Delta G_7 + \Delta G_8$ .

Reaction 7 represents the proton transfer that occurs in the gas phase. The heats of reaction  $\Delta H_7$  calculated using ab initio methods are 513.3, 521.6, 537.1, and 522.9 kJ/mol for CHCA, 2,5-DHB, FA, and SA, respectively. The details of calculations are described in the [Supplementary Material](#). These four matrices exhibit a similar heat of reaction in the gas phase. An additional approximation  $\Delta G_8 \approx \Delta H_8$  is used in the calculations.

The Gibbs free energies of Reactions 6 and 8 are calculated using the polarizable continuum model (PCM) [38] included in the Gaussian 09 computational package. The dielectric constant  $\epsilon$  for polar liquids employed in the PCM was calculated using the Kirkwood-Frohlich equation (Equation 9) and Clausius-Mossotti equation (Equation 10) in our previous study.

$$g\mu^2 = \frac{9kT(\epsilon - \epsilon_\infty)(2\epsilon + \epsilon_\infty)}{4\pi\rho_N \epsilon(\epsilon_\infty + 2)^2} \quad (9)$$

$$\frac{\epsilon_\infty - 1}{\epsilon_\infty + 2} = \frac{4\pi}{3} \alpha' \rho_N \quad (10)$$

However, the most appropriate method for performing dielectric constant  $\epsilon$  calculations has been reported by Caillol et al. [39, 40]:

$$\frac{(\epsilon - 1)(2\epsilon + 1)}{3\epsilon} - \frac{(\epsilon_\infty - 1)(2\epsilon_\infty + 1)}{3\epsilon_\infty} = \frac{4}{3kT} \pi \rho_N g \mu^2 \quad (11)$$

where  $\epsilon_\infty$ ,  $\rho_N$ ,  $\mu$ , and  $k$  are the high-frequency dielectric constant, density, dipole moment, and Boltzmann constant, respectively. The typical values of correlation factor  $g$  for molecules contain an aromatic ring and substitution functions ranging

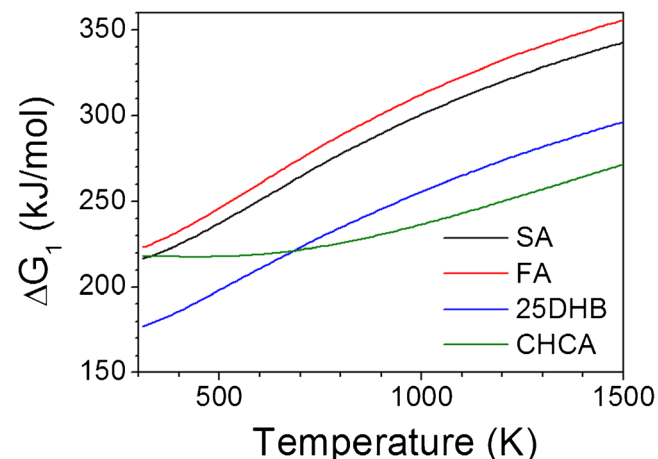


Figure 7. Gibbs free energy of Reaction 1. Only the calculations of  $g=1$  for Equation 11 are shown



from 1 to 2. At high temperatures,  $g$  approaches 1. The approximations  $g=1$  and 2 are used in the calculations. In this study, we use the Caillol equation and Clausius-Mossotti equation for calculating the dielectric constant, although the difference of the dielectric constants calculated using the Kirkwood-Frohlich equation and Caillol equation is small. The polarizabilities  $\alpha'$  and dipole moments  $\mu$  employed in these equations are calculated using the Gaussian 09 computational package (MP2/6-31+G\*\* method). Numerous conformers exist for each matrix, and the dipole moment of each conformer is distinct. The dipole moment for each matrix used in calculating the dielectric constant is the averaged dipole moment of the conformers, weighted by the fraction of the population comprising each conformer. The fraction of the population is calculated according to Boltzmann distribution. By contrast, the polarizability of each conformer is similar. The polarizability of the most stable conformer is used in the calculations of the dielectric constant. The geometries, energies, and dipole moments of the conformers, the temperature-dependent dielectric constant, and the solvation energy are presented in the [Supplementary Material](#).

The Gibbs free energy of Reaction 1 is shown in Figure 7. Generally, the heat of reaction increases with temperature because the dielectric constant decreases as the temperature increases, resulting in a decrease in solvation energy.

The ion-to-neutral ratios derived from the calculations represent the ion-to-neutral ratio in the condensed phase. Because the ion loss from ion-ion recombination and ion generation from the thermal proton transfer reaction are both small in gas plume [20, 21], the ion-to-neutral ratios derived from the calculations are close to the ion-to-neutral ratio of the gas plume after expansion. They are shown in Figure 5 for comparison with the experimental results. The ion-to-neutral ratio of CHCA is approximately three orders of magnitude higher than that of the other three matrices at the same laser fluence. The absorption coefficient of CHCA at 355 nm is 2.8 times higher than that of SA and FA, and 3.7 times higher than that of 2,5-DHB. The calculations indicate that the temperature of CHCA is approximately 2 to 3 times higher than that of the other matrices, as illustrated in Figure 6. The difference in the Gibbs free energy of Reaction 1 among these matrices is only approximately 25%. Therefore, the high ion-to-neutral ratio of CHCA mainly results from the high temperature.

The ion-to-neutral ratios of CHCA, 2,5-DHB, SA, and FA calculated using a thermal proton transfer model indicate an analogous trend and exhibit orders of magnitude that are similar to those derived from experimental measurements. The calculations are performed without using any fitting parameters, and the results provide only an estimated order of magnitude of the ion-to-neutral ratios of the matrices. The difference between the values derived from this model and the experimental measurements is considerably smaller than the difference between the values derived from the other models and the experimental measurements. For example, ion-to-neutral ratios derived from the energy pooling model and the electronically excited matrix model differ by approximately 4 to 5 orders of

magnitude from those derived from the experimental measurements. The findings of this study indicate that thermally induced proton transfer must be the dominant reaction in ion generation that occurs in MALDI processes. Although we do not exclude the possibility that other mechanisms contribute to ion generation, the contribution of those mechanisms are likely to be small.

## Acknowledgments

The authors acknowledge the support of the Thematic Research Program, Academia Sinica, Taiwan (AS-102-TP-A08) and the National Science Council, Taiwan (NSC 100-2113-M-001-026-MY3).

## References

1. Tanaka, K., Waki, H., Ido, Y., Akita, S., Yoshida, Y.: Protein and polymer analyses up to  $m/z = 100,000$  by laser ionization time-of-flight mass spectrometry. *Rapid Commun. Mass Spectrom.* **2**, 151–153 (1988)
2. Karas, M., Hillenkamp, F.: Laser desorption/ionization of proteins with molecular masses exceeding 10,000 Daltons. *Anal. Chem.* **60**, 2299–2301 (1988)
3. Knochenmuss, R.: A quantitative model of ultraviolet matrix-assisted laser desorption/ionization. *J. Mass Spectrom.* **37**, 867–877 (2002)
4. Bae, Y.J., Shin, Y.S., Moon, J.H., Kim, M.S.: Degree of ionization in MALDI of peptides: thermal explanation for the gas-phase ion formation. *J. Am. Soc. Mass Spectrom.* **23**, 1326–1335 (2012)
5. Hillenkamp, F., Karas, M.: In: MALDI MSA Practical Guide to Instrumentation Methods and Applications. Hillenkamp, F., Peter-Katalinic, J. Eds Wiley-VCH Verlag GmbH & Co. KGaA: Weinheim, Germany, pp. 11 (2007)
6. Mowry, C.D., Johnston, M.V.: Simultaneous detection of ions and neutrals produced by matrix-assisted laser desorption. *Rapid Commun. Mass Spectrom.* **7**, 569–575 (1993)
7. Poretzky, A., Geohegan, D.B.: Gas-phase diagnostics and LIF-imaging of 3-hydroxypicolinic acid MALDI-matrix plumes. *Chem. Phys. Lett.* **286**, 425–432 (1998)
8. Ens, W., Mao, Y., Mayer, F., Standing, K.G.: Properties of matrix-assisted laser desorption measurements with a time-to-digital converter. *Rapid Commun. Mass Spectrom.* **5**, 117–123 (1991)
9. Quist, A.P., Huth-Fehre, T., Sundqvist, B.U.R.: Total yield measurements in matrix-assisted laser desorption using a quartz crystal microbalance. *Rapid Commun. Mass Spectrom.* **8**, 149–154 (1994)
10. Dreisewerd, K., Schürenberg, M., Karas, M., Hillenkamp, F.: Influence of the laser intensity and spot size on the desorption of molecules and ions in matrix-assisted laser desorption/ionization with a uniform beam profile. *Int. J. Mass Spectrom. Ion Process* **141**, 127–148 (1995)
11. Breuker, K., Knochenmuss, R., Zhang, J., Stortelder, A., Zenobi, R.: Thermodynamic control of final ion distributions in MALDI: in-plume proton transfer reactions. *Int. J. Mass Spectrom.* **226**, 211–222 (2003)
12. Knochenmuss, R., Zenobi, R.: MALDI ionization: the role of in-plume processes. *Chem. Rev.* **103**, 441–452 (2003)
13. Dreisewerd, K.: The desorption process in MALDI. *Chem. Rev.* **103**, 395–425 (2003)
14. Zenobi, R., Knochenmuss, R.: Ion formation in MALDI mass spectrometry. *Mass Spectrom. Rev.* **17**, 337–366 (1998)
15. Knochenmuss, R.: Ion formation mechanisms in UV-MALDI. *Analyst* **131**, 966–986 (2006)
16. Knochenmuss, R., Zhigilei, L.V.: What determines MALDI ion yields? A molecular dynamics study of ion loss mechanisms. *Anal. Bioanal. Chem.* **02**, 2511–2519 (2012)
17. Tsai, M.T., Lee, S., Lu, I.C., Chu, K.Y., Liang, C.W., Lee, C.H., Lee, Y.T., Ni, C.K.: Ion-to-neutral ratio of 2,5-dihydroxybenzoic acid in matrix-assisted laser desorption/ionization. *Rapid Commun. Mass Spectrom.* **27**, 955–963 (2013)

18. Allwood, D.A., Dyer, P.E., Dreyfus, R.W.: Ionization modeling of matrix molecules in ultraviolet matrix-assisted laser desorption/ionization. *Rapid Commun. Mass Spectrom.* **11**, 499–503 (1997)
19. Park, K.M., Ahn, S.H., Bae, Y.J., Kim, M.S.: *Bull. Korean Chem. Soc.* **34**, 907–911 (2013)
20. Chu, K.Y., Lee, S., Tsai, M.T., Lu, I.C., Dyakov, Y.A., Lai, Y.H., Lee, Y.T., Ni, C.K.: Thermal proton transfer reactions in ultraviolet matrix-assisted laser desorption/ionization. *J. Am. Soc. Mass Spectrom.* **25**, 310–318 (2014)
21. Chu, K.Y., Lee, S., Tsai, M.T., Lu, I.C., Dyakov, Y.A., Lai, Y.H., Lee, Y.T., Ni, C.K.: Erratum to: thermal proton transfer reactions in ultraviolet matrix-assisted laser desorption/ionization. *J. Am. Soc. Mass Spectrom.* **25**, 1087–1087 (2014)
22. Allwood, D.A., Dreyfus, R.W., Perera, I.K., Dyer, P.E.: UV optical absorption of matrices used for matrix-assisted laser desorption/ionization. *Rapid Commun. Mass Spectrom.* **10**, 1575–1578 (1996)
23. Liu, C.L., Hsu, H.C., Ni, C.K.: Time-sliced ion imaging study of  $I_2$  and  $I_2^+$  photolysis at 532 nm. *Phys. Chem. Chem. Phys.* **7**, 2151–2155 (2005)
24. Hsu, H.C., Tsai, M.T., Dyakov, Y.A., Ni, C.K.: Energy transfer of highly vibrationally excited molecules studied by crossed molecular beam/time-sliced velocity map ion imaging. *Int. Rev. Phys. Chem.* **31**, 201–233 (2012)
25. Lee, Y.T., McDonald, J.D., LeBreton, P.R., Herschbach, D.R.: Molecular beam reactive scattering apparatus with electron bombardment detector. *Rev. Sci. Instrum.* **40**, 1402–1408 (1969)
26. Sparks, R.K.: Crossed Beam Studies of Full and Half Collisions. Ph.D. Thesis, University of California, Berkeley (1980)
27. Liang, C.W., Lee, C.H., Lin, Y.J., Lee, Y.T., Ni, C.K.: MALDI mechanism of dihydroxybenzoic acid isomers: desorption of neutral matrix and analyte. *J. Phys. Chem. B* **117**, 5058–5064 (2013)
28. Wiza, J.L.: Microchannel plate detectors. *Nucl. Instrum. Methods* **162**, 587–601 (1979)
29. Houston, P.L.: *Chemical Kinetics and Reaction Dynamics*, 1st ed. McGraw-Hill, New York, pp. 121. (2001)
30. Freund, R.S., Wetzel, R.C., Shul, R.J., Hayes, T.R.: Cross-section measurements for electron-impact ionization of atoms. *Phys. Rev. A* **41**, 3675–3595 (1990)
31. Pedder, R.E., Wei, J.: Quadrupole performance: do quadrupoles discriminate against high masses? Extrel application note GT-315D. Extrel CMS: Pittsburgh, PA, USA (n.d.)
32. Beran, J.A., Kevan, L.: Molecular electron ionization cross sections at 70-eV. *J. Phys. Chem.* **73**, 3866–3876 (1969)
33. NIST Physical Measurement Laboratory. Available at: <http://www.nist.gov/pml/data/ionization/index.cfm>. Accessed 30 Jul 2014
34. Bull, J.N., Harland, P.W., Vallance, C.: Absolute total electron impact ionization cross-sections for many-atom organic and halocarbon species. *J. Phys. Chem. A* **116**, 767–777 (2012)
35. Knochenmuss, R.: Energetics and kinetics of thermal ionization models of MALDI. *J. Am. Soc. Mass Spectrom.* **25**, 1521–1527 (2014)
36. Gray-Weale, A., Ni, C.K.: Comment on “Energetics and Kinetics of Thermal Ionization Models of MALDI”. (submitted as a supplementary material for reviewers; also submitted to *J. Am. Soc. Mass Spectrom.* in August 26, 2014 as a separate article, accepted)
37. Lide, D.R.: *CRC Handbook of Chemistry and Physics*. CRC Press, Boca Raton (1993)
38. Tomasi, J., Mennucci, B., Cammi, R.: Quantum mechanical continuum solvation models. *Chem. Rev.* **105**, 2999–3093 (2005)
39. Caillol, J.M., Levesque, D., Weis, J.J.: Electrical properties of polarizable ionic solutions. I. Theoretical aspects. *J. Chem. Phys.* **91**, 5544–5554 (1989)
40. Caillol, J.M., Levesque, D., Weis, J.J.: Electrical properties of polarizable ionic solutions. II. Computer simulation results. *J. Chem. Phys.* **91**, 5555–5566 (1989)